Prompt core confinement improvement across the L H transition in DIII-D: Profile stiffness, turbulence dynamics, and isotope effect

Prompt core confinement improvement across the L-H transition in DIII-D: profile stiffness, turbulence dynamics, and isotope effect

T. Kobayashi[1,2], Z. Yan[3], G. R. McKee[3], M. E. Austin[4], B. A. Grierson[5], and P. Gohil[5]

[1] National Institute for Fusion Science, National Institutes of Natural Sciences, Toki 509-5292, Japan

[2] The Graduate University for Advanced Studies, SOKENDAI, Toki 509-5292, Japan

[3] University of Wisconsin-Madison, Madison, WI 53706, United States of America

[4] University of Texas, Austin, TX 78712, United States of America

[5] General Atomics, San Diego, CA 92186, United States of America

E-mail: kobayashi.tatsuya@nifs.ac.jp

Abstract. We elaborate on the nature of the prompt core confinement improvement observed at the L-H transition in DIII-D, which is a long-standing issue unsolved for more than two decades and can impact future fusion reactor performance. Dynamic transport analysis suggests the essential role of the profile stiffness for understanding the mechanism of the prompt core confinement improvement. Beam emission spectroscopy shows that transport reduction at the core cannot be explained only by the ion scale turbulence density fluctuation suppression. Properties of nonlocal confinement improvement across the L-H transition are experimentally assessed in hydrogen (H) and deuterium (D) plasmas. Prompt core confinement improvement is found to be more rapid in the lighter hydrogen isotope.

1. Introduction

After the first discovery of the high confinement mode (H-mode) transition [1], extensive effort has been made to understand the background mechanism of the edge transport barrier (ETB) formation. Although basic properties of the ETB formation, e.g., excitation of the $E \times B$ shear flow [2, 3], turbulence transport suppression [4, 5, 3], and the isotope effects on the threshold condition [6, 7, 8], were successfully understood to a certain extent, some important enigmas still remain unresolved. One of these conundrums is the prompt core confinement improvement across the low to high confinement mode transition (L-H transition) [9, 10, 11]. That is, although the radial electric field as the turbulence regulator is only excited in a limited peripheral region [12], the turbulent transport is nonlocally suppressed in a wide radial region including the core. The nonlocal transport observed in L-mode plasmas [13] is considered to have a link to the prompt core confinement improvement. Physics-based profile prediction in the H-mode core is extremely valuable for elaborated projection of future thermonuclear fusion reactor performance [14].

In this paper, the prompt core confinement improvement across the the L-H transition in DIII-D is studied. Dynamic transport analysis suggests the essential role of the profile stiffness [15, 16] for understanding the mechanism of the prompt core confinement improvement. It is indicated that the transport reduction at the core cannot be explained only by the ion scale turbulence density fluctuation suppression experimentally measured. Motivated by the clear isotope effect in the L-H transition

power threshold [6, 7, 8], properties of nonlocal confinement improvement across the L-H transition are experimentally assessed in hydrogen (H) and deuterium (D) plasmas for the first time. Prompt core confinement improvement is found to be more rapid in the lighter hydrogen isotope.

2. Results

The experiments were conducted on the DIII-D tokamak with neutral beam (NB) heated ITER similar shape plasmas [7]. The toroidal magnetic field B_{t} is 2.1 T with the ion ∇B drift towards the X-point. The safety factor at the 95 % magnetic flux surface q_{95} is set to be 5 with the plasma current I_{p} of 1 MA. Before the L-H transition, the line averaged density $\bar{n}_{\mathrm{e}}$ is maintained to be 3×10^{19} m^{-3}. In addition to regular D plasma discharges, H plasmas are generated by H beam and H puff with a high H purity more than 92 % in a dedicated campaign. For the transport analysis discussed below, the electron temperature evolution is measured by the high time resolution electron cyclotron emission (ECE) radiometer, where the signal is cross-calibrated by the Thomson scattering (TS) data. Ion scale turbulent density fluctuation is measured by the beam emission spectroscopy (BES) [17] in a one-dimensional radial array covering $0.65 < \rho < 1$, where $\rho = \sqrt{\Psi_{\mathrm{N}}}$ and Ψ_{N} is the normalized toroidal flux.

Figure 1 shows the typical time evolution of the hydrogen target discharge. For finding the L-H transition power threshold, the NB power is increased stepwise at the current and density flattops. The L-H transition time is $t_{\mathrm{LH}} = 1736.1$ ms manifested by

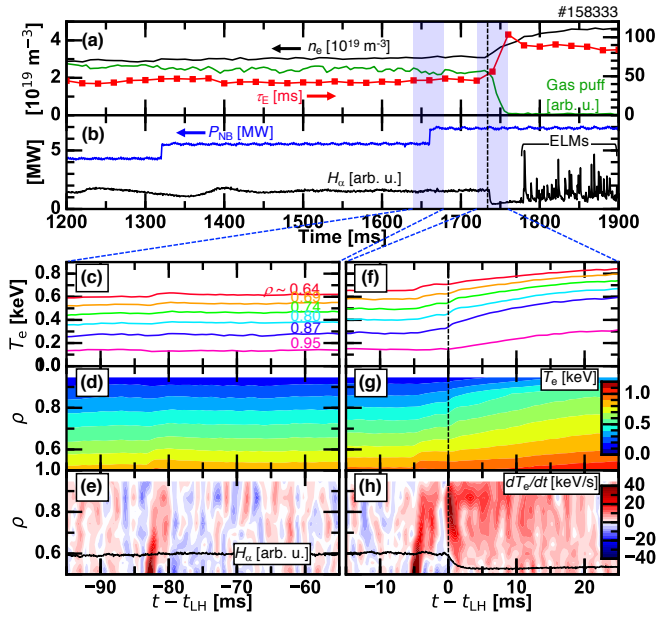

Figure 1. Time evolutions of (a) the line averaged density, the gas injection rate, and the energy confinement time, (b) the neutral beam power and the H_α emission intensity, and (c,f) the electron temperature traces at various radii; and spatiotemporal evolutions of (d,g) the electron temperature and (e,h) the time derivative of the electron temperature with H_α emission intensity overlaid in the L-mode phase and across the L-H transition, respectively. The vertical dashed line indicates the L-H transition time of $t_{\mathrm{LH}} = 1736.1$ ms.

the drops in the edge H_α signal and the feedback-controlled gas injection rate as well as the abrupt increases in the energy confinement time and the line averaged density [Figs. 1 (a,b)]. Radial profiles of the electron density n_e and the electron temperature T_e measured by the TS are shown in Figs. 2 (a,b), respectively. Before the L-H transition, the n_e profile is peaked and no apparent pedestal structure exists in the T_e profile. Once the L-H transition occurs, clear pedestal structures appear in the n_e profile and the T_e profile at the peripheral region $\rho > 0.95$. Quick increase in the quantities at the peripheral region leads to the profile flattening at the inner side of the pedestal both in

n_e ($\rho > 0.5$) and in T_e ($\rho > 0.7$). The location of the sheared $E \times B$ flow structure is determined as $\rho > 0.85$ by the charge exchange recombination spectroscopy.

Spatiotemporal evolution of T_e measured by the ECE and its time derivative $\partial T_e/\partial t$ in the L-mode phase and across the L-H transition are shown in Figs. 1 (c-h). The radial region of interest, $0.6 < \rho < 1$, is covered by six channels, having a radial interspacing of $\sim$ 2.5 cm. For suppressing the high frequency noise, a numerical low pass filter with the cut-off frequency of 650 Hz, which is much faster than the energy confinement time scale, is applied to the ECE data. In the L-mode phase at $t - t_{LH} \sim -83$ ms, an outward propagation of the increased T_e is observed, which corresponds to the heat pulse induced by a sawtooth crash [Fig. 1 (e)]. Another sawtooth heat pulse is seen at $t - t_{LH} \sim -5$ ms shortly before the L-H transition. Note that the sawtooth inversion radius is far inside ($\rho \sim 0.22$) and the heat pulse is rather less sharp in the edge region. At the L-H transition, an inward propagating pulse of the T_e increase appears as implied in [18], after which T_e continues to increase in a wide radial region. The pulse propagation speed in radius is ~ -115 m/s, which is one order of magnitude smaller than the electron diamagnetic drift velocity (typical propagation speed of the turbulence spreading pulse [19, 20]). This chained sequence of the T_e increase corresponds to the inward transmission of the prompt transport suppression front starting from the edge $E \times B$ shear region.

Firstly, we discuss a possible explanation of the prompt core confinement improvement. The electron heat flux q_e is evaluated from the energy conservation

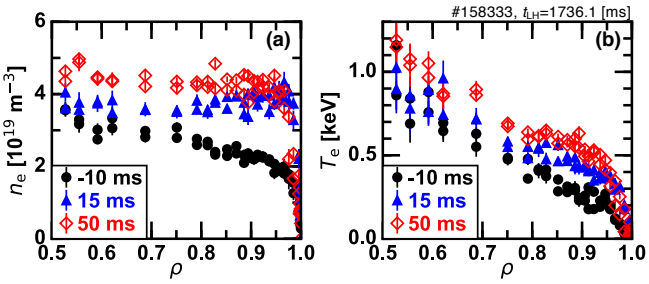

Figure 2. Radial profiles of (a) the electron density and (b) the electron temperature.

equation as $q_{\rm e} = V'^{-1} \int_0^r \left[P - \frac{3}{2}\partial\left(n_{\rm e}T_{\rm e}\right)/\partial t\right] V' dr$, where P is the heating power density including the NB heating, the Ohmic heating, the radiation loss, and the ion-electron temperature equilibration and V' is the radial derivative of the torus volume inside the flux surface labelled by r. Time evolutions of P and V' are calculated by a transport analysis code ONETWO [21]. For obtaining the $n_{\rm e}$ profile evolution, the spatially-smoothed TS data in $t > t_{\rm LH}$ is fitted by $n_{\rm e,fit} = n_{\rm e,L} + \Delta n_{\rm e}[1 - e^{-(t-t_{\rm LH})/\Delta t}]$, where $\Delta n_{\rm e}$ and Δt are the fitting parameters and $n_{\rm e,L}$ is the mean electron density profile in the L-mode, $t < t_{\rm LH}$. As an example, measured data and fitting curves are shown for different radial positions in Fig. 3. Uncertainness of the fitting is considered in the transport analysis below.

Figure 4 (a) is the time evolution of the electron heat flux divided by the electron density $q_{\rm e}/n_{\rm e}$ and the electron temperature gradient $-\nabla T_{\rm e}$ at $\rho \sim 0.74$, far inside the $E \times B$ shear region. Across the L-H transition, $q_{\rm e}/n_{\rm e}$ is quickly suppressed even though the local $E \times B$ shear is considered to remain unchanged. The value without the contribution of $\partial n_{\rm e,fit}/\partial t$ is overlaid by the thin dashed curve to exclude uncertainness of fitting. This dashed curve corresponds to the possible upper boundary of $q_{\rm e}/n_{\rm e}$.

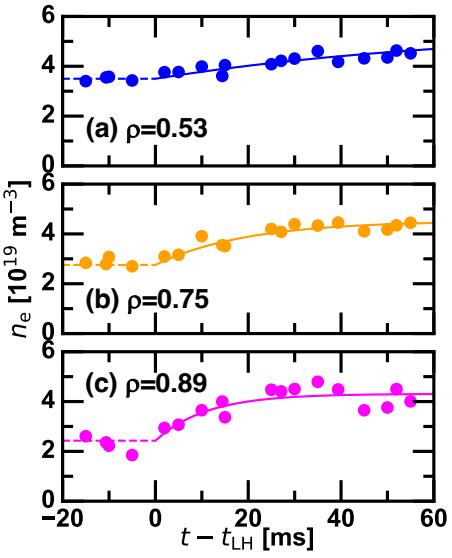

Figure 3. Time evolution of electron density measured by Thomson scattering and exponential fitting at (a) $\rho = 0.53$, (b) 0.75, and (c) 0.89.

Even only with the $\partial T_e/\partial t$ contribution, the prompt reduction of q_e/n_e is reproduced. Slight decrease in $-\nabla T_e$ is due to the drastic increase in T_e at the edge pedestal of $\rho > 0.95$ with a moderate change in T_e in the core as shown in Fig. 1 (f) and Fig. 2 (b). Figure 4 (b) is the flux–gradient diagram, where time is shown by the color bar. Different phases, i.e., L-mode, transition phase, and H-mode, are shown by different symbols, i.e., circles, squares, and triangles, respectively. In addition, points for $t - t_{LH} = -0.9$ and 1.3 ms are specially marked as representative data in L-mode and H-mode. The slope between each point and the origin corresponds to the power balance thermal diffusivity $\chi_e^{PB} = -q_e/(n_e \nabla T_e)$ and the derivative of the points shows the heat pulse thermal diffusivity $\chi_e^{HP} = -\partial(q_e/n_e)/\partial \nabla T_e$ [22]. Across the L-H transition, $\chi_e^{HP} \sim 18$ m^2/s is much larger than $\chi_e^{PB} \sim 3.4$ m^2/s, which corresponds to a representative feature of the profile stiffness [15, 16]. In the presence of the profile stiffness, the slight decrease in

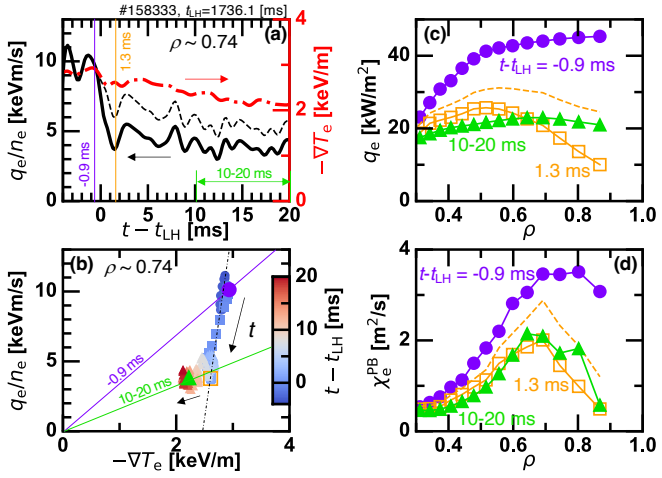

Figure 4. (a) Time evolutions of the electron heat flux divided by the electron density and the electron temperature gradient at $\rho = 0.74$ and (b) its flux–gradient diagram; and radial profiles of (c) the electron heat flux and (d) the electron thermal diffusivity. Thin dashed curves in (a,c,d) correspond the values without considering the electron density evolution. Colored lines and symbols in (b-d) correspond to the data at the time indicated in (a) by the vertical lines.

$-\nabla T_e$ induced by the edge pedestal formation leads to the rapid and drastic drop in q_e/n_e. Then, the transport suppression front propagates inwards in a chain reaction manner. Rapid decrease of the n_e gradient possibly plays a role through an off-diagonal contribution as well, as demonstrated in [23, 24] for the nonlocal transport study. After the prompt reduction in q_e/n_e ceases at $t - t_{LH} = 1.3$ ms, the trajectory in the flux–gradient diagram transits to a different branch with $\chi_e^{HP} \sim \chi_e^{PB}$, i.e., no stiffness.

Figure 4 (c) shows the radial profile of q_e for the specific time slices and the time period. Before the L-H transition, $t - t_{LH} = -0.9$ ms, q_e monotonically increases in radius, which is mainly driven by the NB heating having a wide absorption profile. Shortly after the L-H transition, $t - t_{LH} = 1.3$ ms, q_e is significantly reduced by

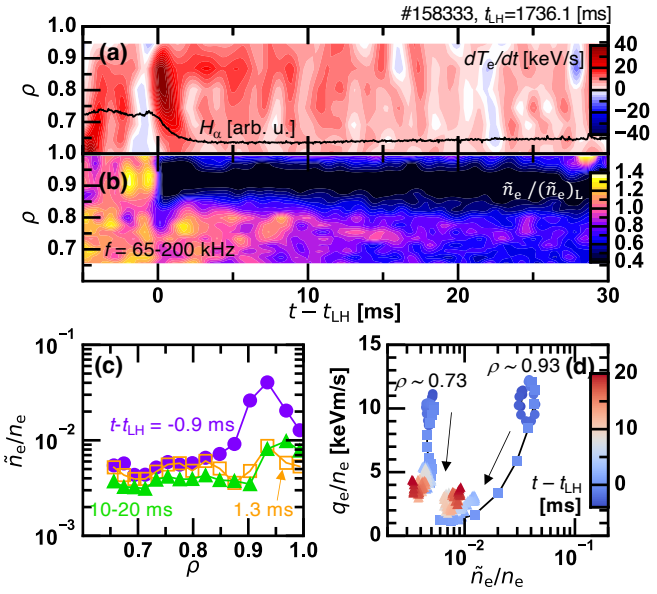

Figure 5. Spatiotemporal evolutions of (a) the time derivative of the electron temperature with H_α emission intensity overlaid and (b) the relative turbulence amplitude with respect to its L-mode value; (c) radial profile of the turbulence amplitude; and (d) relation between the turbulence amplitude and the electron heat flux divided by the electron density.

the positive value of $\partial T_e/\partial t$ in a wide radial region. Even without considering the contribution of $\partial n_{e,fit}/\partial t$, q_e is substantially reduced as shown by the thin dashed curves. In the later time period, $t - t_{LH} = 10 - 20$ ms, q_e remains reduced. Note that the reduced heat flux is maintained in the temperature rising phase and eventually returns to the original value in the confinement time scale. The heat flux in the later H-mode is driven by some other mechanisms under the increased gradient. Evolution of χ_e^{PB} profile shown in Fig. 4 (d) exhibits a similar global reduction across the L-H transition as previously reported in [10].

Next, the role of the ion scale turbulent density fluctuation amplitude $\tilde{n}_e$ on the prompt core confinement improvement is studied through the BES measurement.

Turbulent transport reduction away from the $E \times B$ shear region was previously reported in [25, 5]. Figures 5 (a,b) compare the spatiotemporal evolution of $\partial T_{\rm e}/\partial t$ to that of $\tilde{n}_{\rm e}/(\tilde{n}_{\rm e})_{\rm L}$, where $(\tilde{n}_{\rm e})_{\rm L}$ is the mean turbulence amplitude in the L-mode. The turbulence amplitude is defined by the moving averaged cross power spectrum (CPS) of the density fluctuations measured at radially adjacent sample volumes. The CPS components in the frequency range from 65 kHz to 200 kHz is integrated and the numerical low pass filter used for the ECE signals is applied afterward. In the $E \times B$ shear region of $\rho > 0.85$, $\tilde{n}_{\rm e}/(\tilde{n}_{\rm e})_{\rm L}$ is immediately suppressed. Detailed physics of the turbulence suppression at the ETB region was discussed in [26]. In contrast, further in, substantial reduction in $\tilde{n}_{\rm e}/(\tilde{n}_{\rm e})_{\rm L}$ is not seen, although a temporary decrease appears in $0.75 < \rho < 0.85$. Another gradual diminishing with a slow time scale of $O(10$ ms) is observed in $\rho < 0.85$. The time scale of the slow turbulence decay coincides with the time scale of the local gradient change as shown in Fig. 4 (a). No front propagation in $\tilde{n}_{\rm e}/(\tilde{n}_{\rm e})_{\rm L}$ reduction as reported in [27] is found, therefore the prompt core confinement improvement is not fully explained by the ion scale turbulence measured here. Radial profile of the normalized density fluctuation amplitude $\tilde{n}_{\rm e}/n_{\rm e}$ shown in Fig. 5 (c) confirms the immediate drop in the $E \times B$ shear region of $\rho > 0.85$ and the slower decrease in the inner radii. Relation between the turbulence and the transport is displayed as the $\tilde{n}_{\rm e}/n_{\rm e}$ versus $q_{\rm e}/n_{\rm e}$ diagram in Fig. 5 (d). Here, two radial positions $\rho \sim 0.73$ and 0.93 are chosen for representing turbulence dynamics outside and inside the $E \times B$ shear region, respectively. Radial distance between these two points is ~ 8 cm, which is approximately a hundred times

larger than the ion gyro radius and several times larger than the turbulence correlation length [28]. In the $E \times B$ shear region of $\rho \sim 0.93$, the transport reduction is likely linked with the turbulence reduction. However, outside the $E \times B$ shear region at $\rho \sim 0.73$, only the transport is suppressed without an apparent change in the turbulence. This observation implies that the transport reduction in the core should be accounted for by unmeasured quantities, e.g., the electron temperature fluctuation and its cross phase with respect to the potential fluctuation or higher-wavenumber turbulence not detected by BES, which is sensitive to low-wavenumber density fluctuations. As a quick assessment for the turbulence energy source, inverse gradient lengths of the electron density, electron temperature and ion temperature at $0.8 < \rho < 0.9$ are compared. They are defined as $L_\Psi^{-1} \equiv -\Psi^{-1}\partial\Psi/\partial\rho$, where Ψ is either n_e, T_e, or T_i. In the L-mode phase, they are $L_{n_\mathrm{e}}^{-1} = 1.6$, $L_{T_\mathrm{e}}^{-1} = 4.5$, and $L_{T_\mathrm{i}}^{-1} = 2.8$, therefore, a dominant role of the electron temperature gradient driven turbulence in driving transport is suggested. For more detailed investigation, numerical approach is planed in future.

Lastly, the isotope effect on the prompt core confinement improvement is addressed. Here, the discussion is based on the propagation properties of the inverse time constant of T_e, $\tau_{T_\mathrm{e}}^{-1} \equiv T_\mathrm{e}^{-1}\partial T_\mathrm{e}/\partial t$. Figures 6 (a,b) exemplify spatiotemporal evolutions of $\tau_{T_\mathrm{e}}^{-1}$ for D and H plasmas across the L-H transition. These are routinely reproduced in all discharges in the dataset at a fixed line averaged density of $\bar{n}_\mathrm{e} \sim 3 \times 10^{19}$ m^{-3} and different L-H power threshold loss power P_loss shown in Fig. 7 (a). Here, P_loss is defined as $P_\mathrm{loss} = P_\mathrm{NB} + P_\mathrm{ohmic} - dW/dt - P_\mathrm{rad}$ at the transition, where P_NB is the

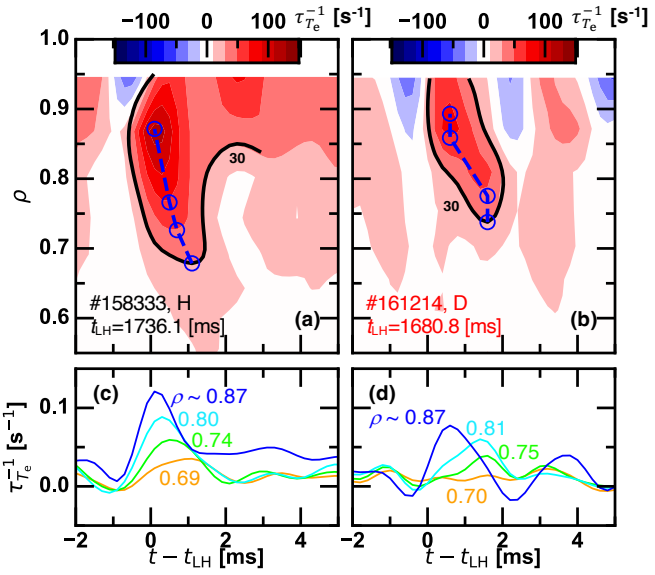

Figure 6. Spatiotemporal evolutions of the inverse time constant of the electron temperature evolution $\tau_{T_e}^{-1}$ in (a) H and (b) D plasmas, and (c) and (d) their time evolutions at specific radii, respectively.

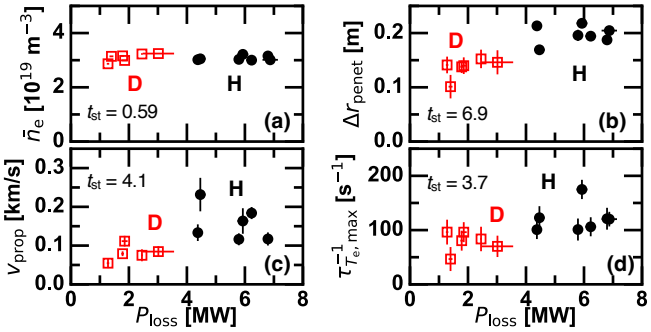

Figure 7. Loss power dependences of (a) the line averaged density and the properties of the prompt core confinement improvement: (b) the penetration depth, (c) the propagation velocity, and (d) the maximum value of $\tau_{T_e}^{-1}$.

NB heating power, P_{ohmic} is the ohmic heating power, W is the plasma stored energy, and P_{rad} is the total radiation loss. Because of the strong isotope dependence in the L-H power threshold, comparison between D and H plasmas at an identical condition cannot be performed. Comparing Figs. 6 (a,b), the H plasma looks to have a faster

and larger magnitude inward propagating $\tau_{T_e}^{-1}$ pulse. For taking a statistical approach, we utilize three different quantities of the propagating $\tau_{T_e}^{-1}$ pulse, i.e., the penetration depth, $\Delta r_{\rm penet}$; the propagation velocity, $v_{\rm prop}$; and the maximum value of $\tau_{T_e}^{-1}$, $\tau_{T_e,\rm max}^{-1}$. We define four specific points to obtain those parameters. The first one is the radius and time of $\tau_{T_e,\rm max}^{-1}$. Following three are the inner most radii and corresponding times in which the contours of $\tau_{T_e}^{-1} = 70$, 50, and 30 $\rm s^{-1}$ reach. These points are shown by blue open circles in Figs. 6 (a,b). The penetration depth is determined by $\Delta r_{\rm penet} = a(1-\rho_{30})$, where a is the minor radius and ρ_{30} is the radius where the contour of $\tau_{T_e}^{-1} = 30$ $\rm s^{-1}$ reaches. The slope of the linear fitting for those four points gives the definition of $v_{\rm prop}$. Those quantities are plotted as a function of $P_{\rm loss}$ for D and H plasmas in Fig. 7. Overall, deeper penetration, faster propagation velocity, and larger value of $\tau_{T_e,\rm max}^{-1}$ are obtained in H plasmas than D plasmas. This can also be interpreted that the pulse having a larger amplitude ($\tau_{T_e,\rm max}^{-1}$) can produce a deeper and faster propagation. In order to prove that the propagation parameters in D and H plasmas are different, the student's t-test is performed. Student's t values, $t_{\rm st}$, for the mean difference between D and H datasets are displayed in each panel. Except for the line averaged density, $t_{\rm st} > 3.7$, indicating the hypothesis that the mean difference is the same is rejected with more than 99 % confidence. This implies that the H plasmas have more significant prompt core confinement improvement than D plasmas. Each of D and H plasmas shows no clear dependence of the propagation properties on $P_{\rm loss}$. Therefore, those differences in D and H plasmas are not merely due to different $P_{\rm loss}$. Improvement of confinement

was more significant in H plasmas according to the TS profile measurement (not shown here for D plasmas). This means that the H plasmas has more room for confinement improvement compared to D plasmas in L-mode, which can be a possible origin for the H/D difference.

As a background mechanism of the prompt core confinement improvement, the turbulence spreading theory [19, 20] is considered. The turbulence spreading theory describes nonlocal turbulence packet transmission across magnetic surfaces having a potential impact on turbulence transport. It was demonstrated in the TJ-II stellarator that turbulence excited at the edge spread into the core region in the L-mode, which was terminated by the edge $E \times B$ shear structure in the H-mode [29]. Here, we also hypothesize that the turbulence spreading is continuously occurring in the L-mode, which enhances the profile stiffness [30]. Once the L-H transition occurs, the turbulence supply into the core is depleted because the turbulence source at the edge region is quenched by the $E \times B$ shear. The improved confinement front is expected to appear as the inward transmission of the turbulent transport reduction. At the same time, local temperature gradient is weakened by temperature increase at the edge-side, which further reduces the local transport and chains the edge and the core. According to the turbulence spreading theory [19, 20], the penetration length and the propagation velocity of a turbulence packet are predicted to be proportional to $\sqrt{D_{\mathrm{T}}}$, where D_{T} is the thermal diffusivity. Considering the isotope effect of confinement [31], D_{T} is generally larger in H plasmas than in D plasmas. Therefore, deeper penetration and faster propagation of

the turbulence packet is expected in H plasmas, as observed experimentally.

Effect of zonal flows is another candidate for the interpretation. As presented in theory [32] and exhibited in numerical simulation [33] and experiment [34], zonal flows are more activated in D plasmas than in H plasmas. With the reinforced zonal flow in D plasmas, the turbulence spreading is expected to be less prominence. Direct detection of zonal flows affected by the isotope mass is a future task.

3. Summary

In this paper, we discussed the properties of the prompt core confinement improvement in DIII-D plasmas. The prompt core confinement improvement was observed as an inward propagation of the increasing rate change in the electron temperature profile. Through the transient transport analysis, an important role of the profile stiffness was pointed out. Ion scale turbulence measurement by the beam emission spectroscopy was performed. Presently, a decoupled dynamics between the heat flux reduction and the turbulence amplitude suppression in the core was observed. For discussing isotope dependence of the properties of the prompt core confinement improvement, propagation velocity and penetration depth of the confinement improvement front were characterized. Faster and deeper propagation of the confinement improvement front was systematically found in hydrogen plasmas than deuterium plasmas.

Acknowledgments

The authors thank C. Petty, S. Smith, and L. Schmitz for useful discussions and one of the authors (T. K.) acknowledges K. Ida, Y. Suzuki, K. Nagasaki, M. Nakata, and S. Sakakibara for strong support. This material is based upon work supported by the U.S. Department of Energy, Office of Science, Office of Fusion Energy Sciences, using the DIII-D National Fusion Facility, a DOE Office of Science user facility, under Awards DE-FC02-04ER54698, DE-FG02-08ER54999, DE-AC02-09CH11466, and DE-FG02-97ER54415. T. K. was also supported by JSPS Core-to-Core Program, A. Advanced Research Networks (PLADyS), JSPS Grant-in-Aid for Scientific Research (17K14898, 21K13902), and Japan–U. S. Cooperation in Fusion Research and Development.

References

[1] F Wagner, G Becker, K Behringer, D Campbell, A Eberhagen, W Engelhardt, G Fussmann, O Gehre, J Gernhardt, G v Gierke, *et al* 1982 *Phys. Rev. Lett.* **49** 1408

[2] L Schmitz 2017 *Nucl. Fusion* **57** 025003

[3] T Kobayashi 2020 *Nucl. Fusion* **60** 095001

[4] R A Moyer, K H Burrell, T N Carlstrom, S Coda, R W Conn, E J Doyle, P Gohil, R J Groebner, J Kim, R Lehmer, *et al* 1995 *Phys. Plasmas* **2** 2397–2407

[5] T Kobayashi, K Itoh, T Ido, K Kamiya, S-I Itoh, Y Miura, Y Nagashima, A Fujisawa, S Inagaki, and K Ida 2017 *Sci. Rep.* **7** 14971

[6] F Ryter, S K Rathgeber, L B Orte, M Bernert, G D Conway, R Fischer, T Happel, B Kurzan, R M McDermott, A Scarabosio, *et al* 2013 *Nucl. Fusion* **53** 113003

[7] Z Yan, P Gohil, G R McKee, D Eldon, B Grierson, T Rhodes, and C C Petty 2017 *Nucl. Fusion* **57** 126015

[8] C F Maggi, H Weisen, J C Hillesheim, A Chankin, E Delabie, L Horvath, F Auriemma, I S Carvalho, G Corrigan, J Flanagan, *et al* 2017 *Plasma Phys. Control. Fusion* **60** 014045

[9] G Becker 1991 *Nucl. Fusion* **31** 663

[10] J G Cordey, D G Muir, V V Parail, G Vayakis, S Ali-Arshad, D V Bartlett, D J Campbell, A L Colton, A E Costley, R D Gill, *et al* 1995 *Nucl. Fusion* **35** 505

[11] H Shirai, T Takizuka, Y Koide, Y Kamada, S Ishida, M Mori, O Naito, M Sato, N Isei, T Fukuda, *et al* 1996 *Plasma Phys. Control. Fusion* **38** 1455

[12] P Gohil, K H Burrell, and T N Carlstrom 1998 *Nucl. Fusion* **38** 93

[13] JD Callen and MW Kissick 1997 *Plasma Phys. Control. Fusion* **39** B173

[14] E Fable, R Wenninger, and R Kemp 2016 *Nucl. Fusion* **57** 022015

[15] F Ryter, G Tardini, F De Luca, H-U Fahrbach, F Imbeaux, A Jacchia, K K Kirov, F Leuterer, P Mantica, A G Peeters, *et al* 2003 *Nucl. Fusion* **43** 1396

[16] J C DeBoo, C C Petty, A E White, K H Burrell, E J Doyle, J C Hillesheim, C Holland, G R McKee, T L Rhodes, L Schmitz, *et al* 2012 *Phys. Plasmas* **19** 082518

[17] G R McKee, C Fenzi, R J Fonck, and M Jakubowski 2003 *Rev. Sci. Instrum.* **74** 2014

[18] L Schmitz, C Holland, T L Rhodes, G Wang, L Zeng, A E White, J C Hillesheim, W A Peebles, S P Smith, R Prater, *et al* 2012 *Nucl. Fusion* **52** 023003

[19] T S Hahm, P H Diamond, Z Lin, K Itoh, and S-I Itoh 2004 *Plasma Phys. Control. Fusion* **46** A323

[20] X Garbet, Y Sarazin, F Imbeaux, P Ghendrih, C Bourdelle, Ö D Gürcan, and P H Diamond 2007 *Phys. Plasmas* **14** 122305

[21] H E St. John, T S Taylor, Y R Lin-Liu, and A D Turnbull 1994 *Plasma Phys. Control. Nucl. Fusion Res.* **3** 603

[22] N J Lopes Cardozo 1995 *Plasma Phys. Control. Fusion* **37** 799

[23] P Rodriguez-Fernandez, A E White, N T Howard, B A Grierson, L Zeng, X Yuan, G M Staebler, M E Austin, T Odstrcil, T L Rhodes, *et al* 2019 *Phys. Plasmas* **26** 062503

[24] C Angioni, E Fable, F Ryter, P Rodriguez-Fernandez, T Pütterich, *et al* 2019 *Nucl. Fusion* **59** 106007

[25] G R Tynan, L Schmitz, R W Conn, R Doerner, and R Lehmer 1992 *Phys. Rev. Lett.* **68** 3032

[26] Z Yan, G R McKee, R Fonck, P Gohil, R J Groebner, and T H Osborne 2014 *Phys. Rev. Lett.* **112** 125002

[27] T Kobayashi, K Itoh, T Ido, K Kamiya, S-I Itoh, Y Miura, Y Nagashima, A Fujisawa, S Inagaki, K Ida, *et al* 2015 *Nucl. Fusion* **55** 063009

[28] G R McKee, R J Fonck, D K Gupta, D J Schlossberg, M W Shafer, R L Boivin, and W Solomon 2007 *Plasma Fusion Res.* **2** S1025

[29] T Estrada, C Hidalgo, and T Happel 2011 *Nucl. Fusion* **51** 032001

[30] S Yi, J M Kwon, P H Diamond, and T S Hahm 2015 *Nucl. Fusion* **55** 092002

[31] M Bessenrodt-Weberpals, F Wagner, O Gehre, L Giannone, J V Hofmann, A Kallenbach, K McCormick, V Mertens, H D Murmann, F Ryter, *et al* 1993 *Nucl. Fusion* **33** 1205

[32] T S Hahm, L Wang, W X Wang, E S Yoon, and F X Duthoit 2013 *Nucl. Fusion* **53** 072002

[33] M Nakata, M Nunami, H Sugama, and T-H Watanabe 2017 *Phys. Rev. Lett.* **118** 165002

[34] Y Xu, C Hidalgo, I Shesterikov, A Krämer-Flecken, S Zoletnik, M Van Schoor, M Vergote, and TEXTOR Team 2013 *Phys. Rev. Lett.* **110** 265005